OXFORD

Phase transitions and degradation/oxidation mechanisms in lead-free CsSnI$_3$ halide perovskites

Alexandra Ivanova[1,*], [iD], Margarita Golikova[1], Lev Luchnikov[1], Pavel Gostishchev[1], Igor Shetinin[1], Victor Voronov[1], Danila Saranin[1] and Vladimir Khovaylo[1,2]

[1]National University of Science and Technology MISIS (NUST MISIS), Leninsky av. 4, Moscow, 119049, Russia
[2]Belgorod State University, Pobedy st. 85, Belgorod, 308015, Russia
*Corresponding author. E-mail: aivanova@misis.ru

Abstract

Halide perovskites possess ultra-low thermal conductivity and show high potential for thermoelectric devices. The chemical properties and molecular structure of halide perovskite materials are not completely stable under ambient conditions, which hinders their use in thermoelectric generators. Changes in the properties of bulk halide perovskite thermoelectrics are accompanied by partial phase transitions and surface oxidation processes. In this paper, we conducted a comprehensive study of the transport and structural properties of CsSnI$_3$, which were pristine by vacuum melting followed by spark plasma sintering. The research results on the electrical transport of these materials revealed that exposure to an inert atmosphere does not deteriorate stability and the properties of the materials remain unchanged. However, prolonged exposure to air leads to a significant degradation of the electrical transport properties. Contrary to thin-film samples, the shift to the double perovskite structure from the perovskite one is limited to a specific surface layer. This change significantly influences the electrical transport of the material while maintaining the essential properties of both perovskite types.

Graphical Abstract
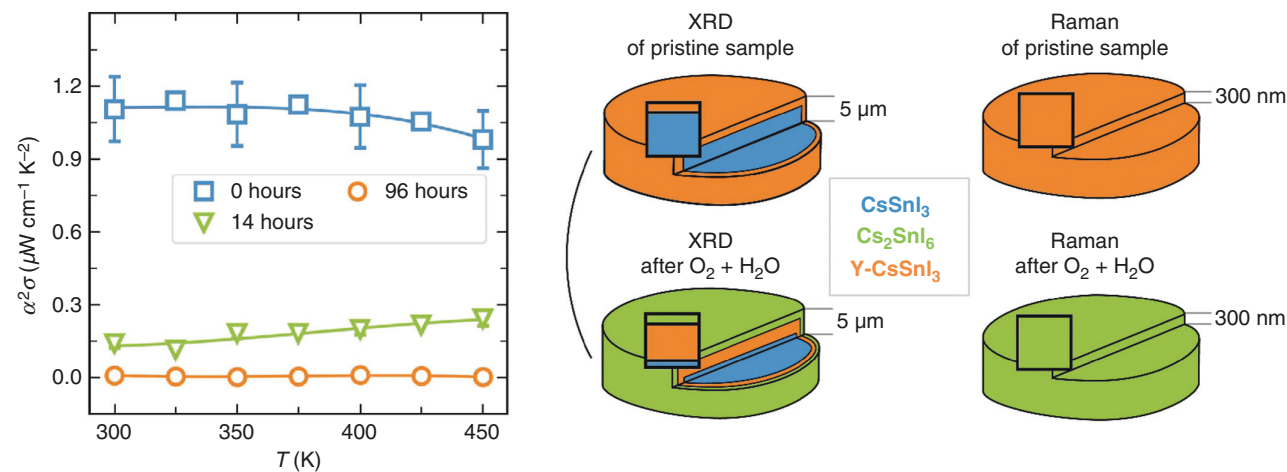
Keywords: halide perovskites; degradation; oxidation; transport properties; surface

Introduction

Thermoelectric (TE) devices, based on the direct conversion of heat into electrical energy, are an essential part of the development of new and environmentally friendly technology for power generation, refrigeration, temperature sensors and thermal management. Since they have the characteristics of high reliability and long operation time, TE energy converters are widely used in the space industry, medical and health care devices, thermoelectric refrigerators, photovoltaic cooling, etc. [1–5].

The maximum efficiency *zT* of a thermoelectric material is defined as:

$$zT = \alpha^2 \sigma T / (\kappa_{lat} + \kappa_{el}) \tag{1}$$

where a is the Seebeck coefficient, σ is the electrical conductivity, and κ_{lat} and κ_{el} are the lattice and electronic thermal conductivities, respectively.

The most effective thermoelectric materials for low-temperature applications, operating within the temperature range of 300–600 K, have been inorganic compounds, specifically bismuth telluride and bismuth selenide [6–8]. Nevertheless, the high costs associated with the fabrication of these materials have prompted a quest for alternative solutions. Despite extensive research into alternative inorganic and organic materials with the potential for high thermoelectric efficiency, their performance notably lags behind that of chalcogenides [9]. This highlights the continuous demand for developing thermoelectric materials that are not only cost-effective, but also efficient, especially for the specified low-temperature range.

In recent years, the appeal of hybrid organic–inorganic and entirely inorganic perovskite materials has grown markedly, finding extensive applications across the spectrum of optoelectronic devices [10–12]. Although lead perovskites have shown superior performance, their toxicity presents a major barrier to commercialization [13, 14]. This has led to an increased focus on research into tin-based perovskites, which, beyond having excellent optical properties, are notable for their exceptionally low thermal conductivity, recorded at <1 Wm^{-1}K^{-1} [15]. Such a characteristic makes them highly attractive for thermoelectric applications.

Miyata *et al.* have classified halide perovskites as having a 'phonon glass, electron crystal' structure [16]. This structural configuration combines the efficient charge transport characteristic of crystals with the phonon thermal conduction inhibition typical of glass [17]. Such a unique property of the material is expected to result in exceptional thermoelectric performance, especially within the realm of lead-free halide perovskites [18]. The inorganic perovskite composition CsSnI$_3$ exhibits a promising combination of semiconductor properties for thermoelectric applications, with a relatively high specific conductivity (~10^1 S/cm at room temperature) and a low band gap (1.25 eV).

The rapid oxidation of Sn^{2+} to Sn^{4+}, when exposed to air or water, limits the development of Sn-based halide perovskites for thermoelectrics. Considerable research efforts have been directed towards stabilizing thin films, aiming to enhance their utility in optoelectronic devices [19–23]. These principles from thin-film research are now being applied to stabilize bulk perovskite materials [24].

However, there is a notable gap in research concerning the oxidation and degradation dynamics within bulk perovskites and their consequent impact on transport characteristics. Conducting such studies on bulk materials is essential to comprehensively evaluate the suitability of perovskites for thermoelectric devices designed for sustained operation under standard conditions.

The inorganic perovskites CsSnI$_3$ have notable attributes in terms of structural stability and chemical composition. The unbalanced presence of different phases of CsSnI$_3$ at room temperature affects the stability of electrical properties during repeated heating and cooling processes [25]. Structural rearrangements of atoms occur during the transitions between phases, leading to macroscopic changes in the structure of the material [26].

The formation of a native oxidized layer can act as a stabilizing passivation film [27]. Hence, it is crucial to investigate the dynamics of changes in the structural and transport properties of bulk CsSnI$_3$ thermoelectrics under cyclic exposure to an external oxidizing environment (air atmosphere) and heating.

In this work, we investigated the correlation between the oxidation/degradation processes and the electrical transport properties of all-inorganic lead-free perovskite CsSnI$_3$. A comprehensive analysis was performed on the evolution of phase composition and the surface state of bulk CsSnI$_3$ semiconductors fabricated using spark plasma sintering. The study evaluated the influence of external corrosion factors (air atmosphere and humidity) by observing structural changes and variations in the elemental composition. The results were evaluated against the stability of transport properties in CsSnI$_3$ (i.e. electrical conductivity) and thermoelectric performance (Seebeck coefficient and power factor).

1 Experimental methods

1.1 Synthesis

The samples of CsSnI$_3$ were synthesized through a meticulous procedure involving vacuum melting and subsequent spark plasma sintering (SPS). High-purity CsI granules (with a purity of 99.998 % from LLC Lanhit, Russia) and SnI$_2$ granules (with a purity of 99.999 % from LLC Lanhit, Russia) were carefully weighed and mixed in stoichiometric proportions within an argon-filled (99.998 % purity) glovebox to prevent contamination and oxidation. The resulting mixtures were hermetically sealed in evacuated quartz tubes with an inner diameter of 10 mm and a wall thickness of 1.5 mm. The sealed tubes were then subjected to a controlled thermal treatment, with a gradual heating to 923 K at a rate of 100 Kh^{-1}, followed by a 24-hour dwell at this temperature and a subsequent gradual cooling to room temperature within the furnace.

The opening of the quartz tubes after melting was carried out in the argon-filled glovebox. Subsequently, the obtained ingots were manually ground into fine powders and subjected to the SPS process under a pressure of 30 MPa at 573 K for a duration of 5 minutes in a vacuum environment. The preparation of the die was also carried out in an argon-filled glovebox and packed in vacuum bags there. This stage allowed the transfer of the die to the SPS unit. After sintering, the dies were again packed into vacuum bags and carried to the glovebox in them. This process yielded fully consolidated bulk cylindrical samples featuring a diameter Ø of 12.7 mm and a thickness of 2 mm.

It is essential to note that the sensitivity of the samples to moisture necessitates stringent precautions throughout both the synthetic and measurement processes. Any contact with solvents or exposure to humidity from the environment should be rigorously avoided to preserve the integrity and properties of the samples.

1.2 Characterization

X-ray diffraction (XRD) patterns were obtained by using a SmartLab diffractometer (Rigaku, Japan) with Cu-Ka radiation (λ = 1.5419 Å). To further examine the morphology and chemical composition of the bulk specimens were employed scanning electron microscopy (Vega 3 SB, Tescan, Czech Republic) and energy-dispersive X-ray spectroscopy (EDX; x-act, Oxford Instruments, UK). Additionally, Raman-scattering data were acquired using a Thermo DXR spectrometer, with excitation provided by a 532-nm laser source. The density of the samples was measured by using the Archimedes principle in isopropyl alcohol, which does not dissolve perovskite. The X-ray photoelectron spectroscopy (XPS) measurements were performed using a «PREVAC EA15» electron spectrometer. In the current work, Al-Ka ($h\nu$ = 1486.6 eV, 150 W)

was used as a primary radiation source. The pressure in the analytical chamber did not exceed 5×10^{-9} mbar during spectra acquisition. The binding energy (BE) scale was pre-calibrated using the positions of Ag $3d_{5/2}$ (368.3 eV) and Au $4f_{7/2}$ (84.0 eV) from silver and gold foils, respectively.

1.3 Transport property measurements

Sample preparation for measurements of electrical transport properties was carried out in an argon-filled glovebox. Consolidated pellets were cut into bars ($3 \times 12.7 \times 2$ mm^3) using a hand-held string saw. Samples were transferred to the set-up without exposure to air in the glovebox. The evaluation included the simultaneous determination of both electrical conductivity σ and the Seebeck coefficient a, employing four-probe and differential techniques, respectively. The measurements were performed under a helium atmosphere in the temperature range of 280–450 K. These analyses were carried out within laboratory-made systems situated at the National University of Science and Technology MISIS. The estimated errors in the Seebeck coefficient and the electrical conductivity measurements are ~8% and ~5%, respectively.

2 Results and discussion

We evaluated the phase composition change of the bulk CsSnI$_3$ sample by investigating the XRD spectra (Fig. S1 in the online Supplementary Data). After exposing the bulk CsSnI$_3$ to an oxidizing air atmosphere (ambient conditions, 22–25°C, 20–45% relative humidity) for different periods, we estimated the dynamics of the phase transitions.

The first measurement of the pristine compressed tablet was taken immediately after its first exposure to the atmosphere after storage in an inert atmosphere. For the 'pristine' sample, we observed two phases: the black Pnam phase of orthorhombic perovskite CsSnI$_3$ (PDF# 01-080-2139) and the yellow Pnma phase of orthorhombic perovskite Y-CsSnI$_3$ (PDF# 01-071-1898). The analysis of the intensity ratio of the main XRD peaks revealed a composition of 79% for the black phase and 21% for the yellow phase of CsSnI$_3$ (Fig. 1). The studies were conducted on bulk samples in tablet form. The attenuation depth of Cu-Ka X-Ray, calculated according to the Beer–Lambert Law, for CsSnI$_3$ is ~5 μm.
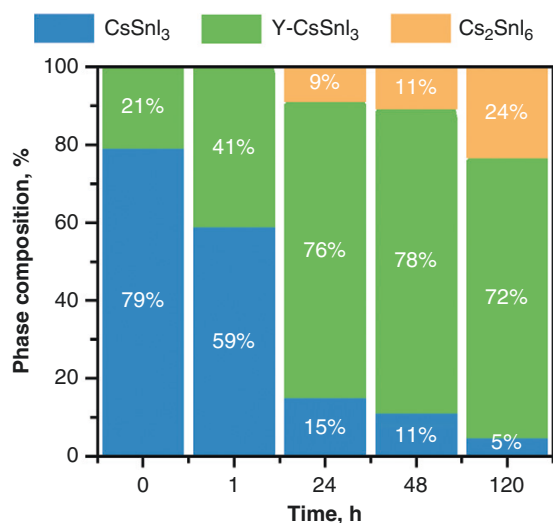
Fig. 1: The phase composition of the CsSnI$_3$ bulk sample, determined by using XRD, following distinct exposure intervals in ambient air

Hence, the presence of a yellow phase in the 'pristine' sample can be related to rapid oxidation processes, even with short-term exposure to air. The content of the Y-CsSnI$_3$ phase significantly increased with the prolonged exposure of the samples to the ambient atmosphere. Upon 24 hours of exposure to oxidation, the Y-CsSnI$_3$ phase evolved to be the dominant phase, representing 76%. In parallel with the phase transition of CsSnI$_3$ from the black to the yellow phase, we observed the appearance of the cubic Cs$_2$SnI$_6$ (PDF# 01-073-0330). This process points to the oxidation process of Sn^{2+} to Sn^{4+} [28]. Continuous exposure of the sample for 120 hours resulted in a change in the phase composition, with an increase in the ratio for Cs$_2$SnI$_6$ (up to 24%), a slight decrease in Y-CsSnI$_3$ (up to 72%) and a significant decrease for black CsSnI$_3$ (5%).

To analyse the compositional changes on the surface of bulk CsSnI$_3$ samples, we conducted Raman spectroscopy measurements (Fig. 2). The penetration depth of visible light (wavelength = 532 nm) for CsSnI$_3$ is submicron (<300 nm) (calculated as the depth of field of the microscope).

The spectra were acquired using backscattering geometry, employing a diffraction grating with 1200 lines/mm and a rectangular aperture measuring 50×1000 μm. A solid-state laser with a wavelength of 532 nm served as the source for the laser radiation, which was concentrated through a 100× objective lens featuring a 0.75 numerical aperture. The power conversion at the sample site was 3 mW, with each exposure spanning 5 seconds and conducted 12 times.

Due to rapid surface oxidation, measurements were taken at short intervals initially in the 'pristine' state and then after 5 minutes, 15 minutes, 4 hours and 24 hours of ambient exposure. For the surface of the pristine sample, we observed the peaks of Y-CsSnI$_3$ at 135, 125 and 89 cm^{-1} [29]. After 15 minutes of external exposure, we observed the appearance of SnI$_4$ and Sn(OH)$_4$, as indicated by the characteristic peaks at 145 and 108 cm^{-1} as the products of perovskite dissolution in air moisture. The presence of oxidation and hydrolysis products highlights interactions with moisture and atmospheric oxygen [30, 31]. After 24 hours of exposure to ambient conditions, high-intensity peaks were identified only for the oxidation products, while the signals for Y-CsSnI$_3$ were almost indistinguishable.

We utilized XPS with Al-Ka emission to precisely analyse the surface properties of the samples. The spectra were calibrated using the C 1s line with an assigned BE of 285.0 eV. A reference sample in the 'pristine' configuration was kept in an inert atmosphere before measurement, briefly exposed to ambient air for no more than 10 seconds upon loading into the vacuum chamber of the XPS system. The investigation into the impact of the oxidation processes was conducted following the 96-hour storage of the sample in an atmospheric air environment with a 20% humidity level. We examined the variations in elemental composition analysis (Table S1 in the online Supplementary Data) based on the integrated intensity of the C 1s, O 1s, Sn $3d_{3/2}$ and Cs $3d_{3/2}$ peaks, considering their respective sensitivity factors of 1, 2.93, 25.05 and 16.46. The increased carbon concentration in the initial sample can be attributed to the conditions of the SPS, which involved interaction with the carbon matrix. Both samples exhibit an imbalance in Cs, Sn and I concentrations compared with the stoichiometric composition of the bulk CsSnI$_3$ sample. The atomic concentration of tin was found to be 6.6 and 6.9 times greater than that of caesium. We propose that the excess tin present on the surface engages in a reaction with oxygen.
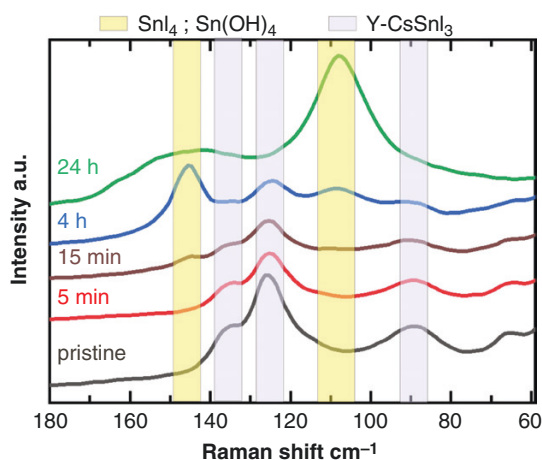
Fig. 2: Raman spectra of the sample with nominal composition of CsSnI₃ following distinct exposure intervals in ambient air

Table 1: Exposure time, actual composition (from the EDX analysis), phase composition and relative density d of the $CsSnI_3$ following exposure intervals in ambient air

Exposure time (h)	Actual composition	Phase composition (wt%)	d (g cm⁻³)
0	$Cs_{0.94}Sn_{1.04}I_{3.02}$	79% $CsSnI_3$, 21% Y-$CsSnI_3$	4.45
1	$Cs_{0.92}Sn_{1.06}I_{3.02}$	58.8% $CsSnI_3$, 41.2% Y-$CsSnI_3$	4.46
24	$Cs_{0.94}Sn_{1.04}I_{3.02}$	14.9% $CsSnI_3$, 76.1% Y-$CsSnI_3$, 9.1% Cs_2SnI_6	4.47
48	$Cs_{0.94}Sn_{1.02}I_{3.04}$	10.7% $CsSnI_3$, 78.6% Y-$CsSnI_3$, 10.7% Cs_2SnI_6	4.55
120	$Cs_{0.94}Sn_{1.02}I_{3.04}$	4.5% $CsSnI_3$, 72% Y-$CsSnI_3$, 23.5% Cs_2SnI_6	4.33

In the case of tin, which exhibits only slight chemical shifts, the chemical state is typically assessed through the modified Auger parameter (*a'*). This parameter is the total of the kinetic energy for one of the leading Auger peaks plus the BE for the primary photoelectron line, formulated as $a' = E_{MNN} + E_{BE}$. Here, E_{MNN} is the peak position of the Auger emission in the kinetic energy domain and E_{BE} represents the BE for the photoelectron line. Fig. S2 (in the online Supplementary Data) presents the spectra in the Sn 3*d* and Sn$_{MNN}$ regions. For the pristine sample, the modified Auger parameter (*a'*) was determined to be 919.45 ± 0.6 and, for the sample after 96 hours, it was 919.36 ± 0.6. These results indicate that the chemical state of the tin on the surfaces of both samples is identical. The absolute *a'* values, as depicted in the Wagner plot, suggest that tin in the sample exhibits an oxidation state intermediately between those of SnO and SnO₂ (valences of +2 and +4, respectively) [32]. The O 1*s* spectra, as illustrated in Fig. S3 (in the online Supplementary Data), reveal the existence of two distinct types of metal(Me)–oxygen bonds: Me–O–H, characterized by a peak at 532.6 eV and Me–O, evident at 531 eV. This observation can be ascribed to the formation of tin oxides (SnO and SnO₂) and tin hydroxide (Sn(OH)₄) on the surfaces of both pristine and aged samples. The performed analysis demonstrates that minimal contact with the atmosphere induces alterations in the surface properties of CsSnI₃ perovskites, suggesting that the oxidation process commences instantaneously upon exposure.

Elemental analysis (Figs S4–S8 in the online Supplementary Data and Table 1), provided via EDX of the sample surfaces during prolonged exposure to air, confirmed the presence of areas with elevated tin and oxygen content. EDX mapping of the specimens revealed a consistent distribution of elements in the sample without air exposure (Fig. S4 in the online Supplementary Data). Energy-dispersive analysis established a congruence between the elemental composition and the nominal composition.

As the air exposure time extended, the elemental ratio was maintained, with the only noticeable change being an increase in oxygen on the surface (Figs S5–S8 in the online Supplementary Data). Surface embrittlement was observed after 24 hours and became more severe with increased exposure. Furthermore, spectroscopic results after 48 hours revealed the emergence of a secondary phase, mainly tin-based, suggesting the potential presence of SnI₄. The prevalence of these tin-rich secondary phases grew with prolonged exposure.

Electrical transport property measurements were performed in both heating and cooling regimes. To verify the stability of the fabricated and estimate its reproducibility, we executed several thermal cycles (Fig. S9 in the online Supplementary Data). The electrical conductivity exhibits metal-like behaviour over the entire temperature range (Fig. 3a). The enhancement in electrical conductivity observed in the perovskite material after 14 hours of ambient air exposure is attributed to intrinsic self-doping processes in tin-based perovskites [22, 33]. This phenomenon involves the oxidation of Sn²⁺ to Sn⁴⁺, resulting in a rise in the concentration of charge carriers [34]. This process leads to a noticeable increase in electrical conductivity. However, after 96 hours of storage under ambient conditions, the electrical conductivity of the material sharply decreases, likely attributed to a reduction in charge-carrier mobility [35]. According to the provided EDX mapping and Raman spectroscopy data, clusters of SnI₄ phase are formed on the surface of the bulk CsSnI₃ sample during oxidation and partial decomposition. These clusters may serve as scattering centres with a low charge-carrier mobility of 2 cm²V⁻¹s⁻¹ at room temperature [36]. Furthermore, the reduced mobility of the charge carriers can be linked to the embrittlement of the CsSnI₃ material.

Conversely, the stability of the Seebeck coefficient during extended air exposure suggests a notable decrease in charge-carrier mobility (Fig. 3b). The electrical properties of CsSnI₃ in its black phase, characterized by *p*-type conductivity [37, 38], distinctly differed from the *n*-type conductivity of the double perovskite Cs₂SnI₆ [39]. Following an extended exposure to ambient air for 4 days, the Seebeck coefficient values consistently displayed positivity, indicating persistent *p*-type conductivity in the samples. This consistent behaviour suggests the presence of a surface passivation phenomenon within the bulk CsSnI₃ material. Although passivation results in a marked reduction in electrical conductivity, it does not affect the conductivity type. Similar property changes were not observed in thin-film configurations of CsSnI₃. According to the literature [40], complete conversion of CsSnI₃ into Cs₂SnI₆ can occur in short periods of ≤48 hours of storage in an air atmosphere. This observation highlights the complex relationship between material morphology, surface interactions and electrical behaviour, revealing promising paths for modifying perovskite materials to suit a range of applications.

Comparing the obtained data with existing literature proves challenging (Fig. S10 in the online Supplementary Data). We examine several significant experimental investigations into the thermoelectric properties of halide perovskites. In the research conducted by Yu *et al.* and Qian *et al.*, bulk samples were
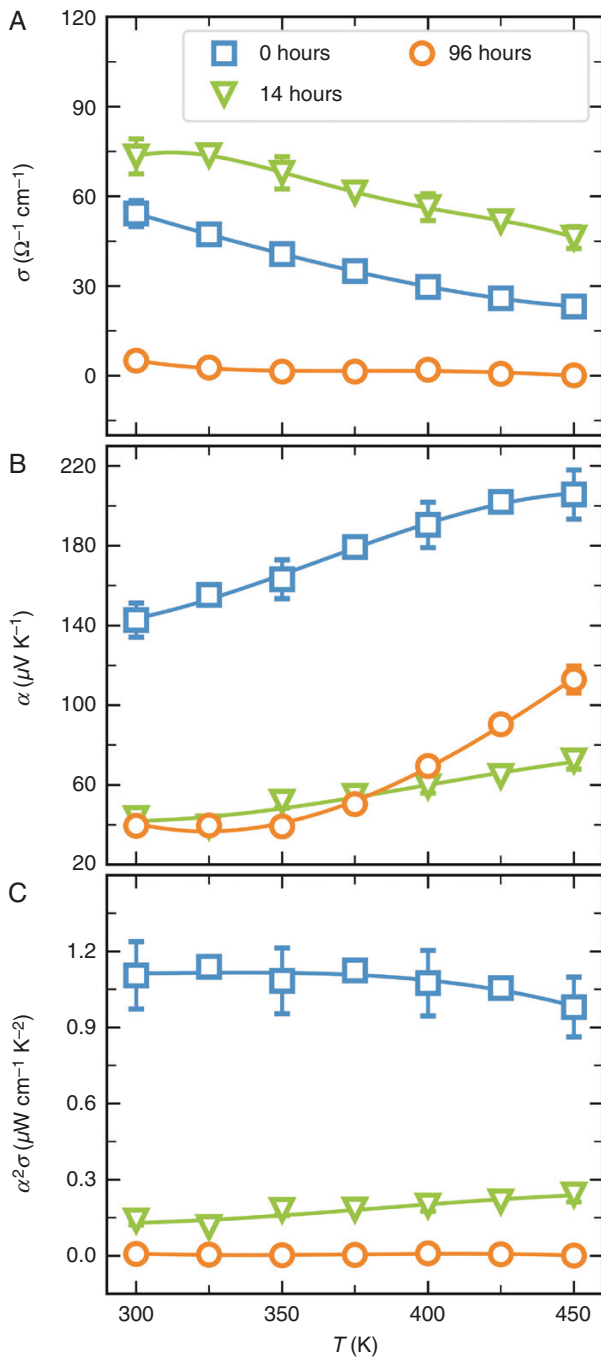
Fig. 3: Temperature dependence of (a) the electrical conductivity σ, (b) the Seebeck coefficient a and (c) the power factor $a^2\sigma$ for the CsSnI₃

synthesized under nearly identical conditions using vacuum melting and analysed using with similar set-ups. However, it was not specified whether the samples were exposed to air prior to measurement [24, 38]. The reported values of electrical conductivity 84–86 $\Omega^{-1}cm^{-1}$ and the Seebeck coefficient 123–124 μV K^{-1} at room temperature in these studies exhibit similarity to the values obtained for pristine sample (53 $\Omega^{-1}cm^{-1}$ and 143 μV K^{-1}) in our work (Table 2). In our investigation, the ingots, post vacuum melting, were processed by grinding and then consolidated via the SPS method. As a result, the electrical conductivity of our samples was 35% lower and the Seebeck coefficient was 15% higher compared with the actual literature, showing a gen-

erally good agreement. The slight discrepancy could stem from differences in the structure of the sample, heavily influenced by the synthesis method or potential exposure to air during sample transportation to the measurement set-ups.

In the study by Xie *et al.*, the synthesis method differed only in the consolidation temperature, with the authors noting that the samples were not exposed to air for >3 minutes [37]. However, the electrical conductivity values of 295 $\Omega^{-1}cm^{-1}$ obtained in this study at room temperature exceeded those reported by Yu *et al.*, Qian *et al.* and our study by 75–85%, while the Seebeck coefficient was three times lower (Table 2 and Fig. S10 in the online Supplementary Data). Such a significant difference in values may indicate material degradation. Although the Seebeck coefficient value after 14 hours of exposure (44 μV K^{-1}) was comparable to that reported by Xie *et al.* (48 μV K^{-1}), the electrical conductivity values, whether for bulk samples or thin films, were not as high [22, 41, 42]. Properties of thin-film materials are heavily dependent on the synthesis method; however, as previously noted, oxidation/degradation processes occur much faster in them than in bulk materials. Therefore, this discrepancy may be attributed to varying degrees of material oxidation/degradation during measurement. These observations underscore the critical necessity of accounting for the absence of any interaction with air when investigating the stability of perovskite materials.

Despite retaining characteristics of both CsSnI₃ and Cs₂SnI₆, the power factor $a^2\sigma$ of the material after prolonged exposure drops to ~10^{-3} μW $cm^{-1}K^{-2}$, contrasting sharply with the value of 1.2 μW $cm^{-1}K^{-2}$ observed in the fresh sample (Fig. 3c).

3 Summary and conclusions

We investigated the evolution of the structural, chemical and transport properties of bulk CsSnI₃ (cylinders with a diameter of 12.7 mm and a thickness of 2 mm) fabricated by using SPS. Analysis using XRD and Raman spectroscopy demonstrated rapid changes in phase composition, as well as oxidation and decomposition processes for the surface regions under ambient conditions. The phase composition changes occurred in several stages and directly correlated with the duration of air exposure. In the 'pristine' sample, the predominant phase was the black Pnam phase of orthorhombic perovskite CsSnI₃. After 24 hours of air storage, the primary phase on the surface of the bulk CsSnI₃ changed to the yellow orthorhombic perovskite Pnma (76%). These phase transitions were accompanied by oxidation linked to the conversion process of Sn²⁺ to Sn⁴⁺. The elemental composition calculations indicated that the Cs₂SnI₆ phase content reached 9.1% after 24 hours and subsequently rose to 23.5% after 120 hours. By employing Raman spectroscopy, the surface composition changes were elucidated, uncovering the existence of decomposition products resulting from hydrolysis and oxidation. The formation of SnI₄ and Sn(OH)₄ occurred within a short exposure period of <1 hour.

The exposition under the ambient conditions enhanced conductivity because of self-doping processes involving Sn²⁺ oxidation to Sn⁴⁺ and raising the concentration of the charge carriers. After 96 hours, conductivity significantly dropped because of scattering effects on the oxidized surface caused by the presence of the decomposition products (SnI₄). The decrease in charge-carrier mobility was also associated with the embrittlement of bulk CsSnI₃ and the spread of surface oxidation effects. The calculation of the Seebeck coefficient in Y-CsSnI₃ showed persistent p-type conductivity even after prolonged exposure, suggesting surface passivation effects. Despite decreased electrical conductivity, the

Table 2: Comparison of representative electrical conductivity σ and Seebeck coefficient a of $CsSnI_3$ determined by using experimental methods

Sample	Synthesis methods	σ, Ω⁻¹cm⁻¹ (room temperature)	α, μV K⁻¹ (room temperature)	Reference
$CsSnI_3$ (this work)	Vacuum melting and spark plasma sintering	53	143	–
$CsSnI_3$ (bulk)	Vacuum melting	86	123	[38]
$CsSnI_3$ (bulk)	Vacuum melting	84	124	[24]
$CsSnI_3$ (bulk)	Vacuum melting and spark plasma sintering	295	48	[37]
$CsSnI_3$ (film)	Mechanochemical synthesis and single-source vacuum deposition	41	27	[41]
$CsSnI_3$ (film)	Spin-coating technique	105	106	[42]
$CsSnI_3$ (film)	Thermal vapour deposition	8	155	[22]

conductivity type remained unchanged. The findings highlight the complexity of tailoring perovskite material properties for diverse applications, considering material morphology, surface interactions and synthesis methods. The stabilization of the conductivity performance after the formation of the oxidized surface areas and phase transformation demonstrates the high potential of bulk $CsSnI_3$ thermoelectrics, as well as the necessity for the development of passivation techniques. We assume that the development of vapour (chemical vapour transport, plasma-enhanced chemical vapour deposition (CVD)) or sputtering methods for the growth of an encapsulation coating could provide long-term stability of the bulk $CsSnI_3$. CVD can be used effectively to form the passivation layer at low temperatures by utilizing π-conjugated ligands (e.g. phenylethylammonium) that stabilize the Sn^{2+} state [43]. The application of passivation and gas-tight coatings, such as Si_3N_4, AlN and SiO_2, is feasibly accomplished using ion-beam deposition. This method ensures the complete uniformity of the coating and eliminates any direct plasma–material interactions, which are unfavourable for processing with halide perovskites [44]. Potentially, the development of encapsulation coatings typically utilized in electronic materials can be tailored to the specific properties of halide perovskites via advanced deposition methods.

Supplementary data

Supplementary data is available at *Clean Energy* online.

Author contributions

A. I.: Data Curation, Formal Analysis, Investigation, Methodology, Writing (Original Draft), Writing (Review & Editing), Visualization. M. G.: Investigation, Visualization. L. L.: Data Curation, Formal Analysis, Investigation, Visualization, Writing (Original Draft), Writing (Review & Editing). P. G.: Investigation, Project Administration, Supervision. I. S.: Investigation. V. V.: Investigation. D. S.: Conceptualization, Supervision, Writing (Review & Editing). V. K.: Writing (Review & Editing), Supervision.

Conflict of interest statement

None declared.

Funding

Data Availability

The data that support the findings of this study are available within the article and its supplementary material.

References

[1] Hendricks T, Caillat T, Mori T. Keynote review of latest advances in thermoelectric generation materials, devices, and technologies 2022. *Energies*, 2022, **15**:7307.

[2] Hu B, Shi X-L, Zou J, *et al.* Thermoelectrics for medical applications: progress, challenges, and perspectives. *Chem Eng J*, 2022, **437**:135268.

[3] Chandel R, Singh Chandel S, Prasad D, *et al.* Review on thermoelectric systems for enhancing photovoltaic power generation. *Sustainable Energy Technol Assess*, 2022, **53**:102585.

[4] Hameed MM, Mansor M, Azrin Mohd Azau M, *et al.* Thermoelectric cooler performance enhancement using thermoelectric generators and their use as a single model to improve the performance of thermal battery management systems for electric vehicles. *Energy Storage*, 2023, **5**:e406.

[5] Liu J, Liu Q, Lin S, *et al.* Wearable thermoelectric generators: materials, structures, fabrications, and applications. *Phys Status Solidi Rapid Res Lett*, 2023, **17**:2200502.

[6] Witting IT, Chasapis TC, Ricci F, *et al.* The thermoelectric properties of bismuth telluride. *Adv Electron Mater*, 2019, **5**:1800904.

[7] Witting IT, Ricci F, Chasapis TC, *et al.* The thermoelectric properties of n-type bismuth telluride: bismuth selenide alloys $Bi_2Te_{3-x}Se_x$. *Research (Wash, D.C.)*, 2020, **2020**:4361703.

[8] Zulkepli N, Yunas J, Mohamed MA, *et al.* Review of thermoelectric generators at low operating temperatures: working principles and materials. *Micromachines*, 2021, **12**:734.

[9] Mao J, Chen G, Ren Z. Thermoelectric cooling materials. *Nat Mater*, 2021, **20**:454–461.

[10] Vats G, Hodges B, Ferguson AJ, *et al.* Optical memory, switching, and neuromorphic functionality in metal halide perovskite materials and devices. *Adv Mater*, 2023, **35**:2205459.

[11] Ai B, Fan Z, Wong ZJ. Plasmonic–perovskite solar cells, light emitters, and sensors. *Microsyst Nanoeng*, 2022, **8**:5.

[12] Saikia D, Betal A, Bera J, *et al.* Progress and challenges of halide perovskite-based solar cell: a brief review. *Mater Sci Semicond Process*, 2022, **150**:106953.

[13] Dou J, Bai Y, Chen Q. Challenges of lead leakage in perovskite solar cells. *Mater Chem Front*, 2022, **6**:2779–2789.

[14] Dissanayake PD, Yeom KM, Sarkar B, *et al.* Environmental impact of metal halide perovskite solar cells and potential

mitigation strategies: a critical review. *Environ Res*, 2023, **219**:115066.

[15] Jin H, Li J, Iocozzia J, *et al*. Hybrid organic–inorganic thermoelectric materials and devices. *Angew Chem Int Ed*, 2019, **58**:15206–15226.

[16] Miyata K, Atallah TL, Zhu X-Y. Lead halide perovskites: crystal-liquid duality, phonon glass electron crystals, and large polaron formation. *Sci Adv*, 2017, **3**:e1701469.

[17] Slack G. *CRC Handbook of Thermoelectrics*. Boca Raton, FL, USA: CRC Press, 1995.

[18] Herz LM. Charge-carrier mobilities in metal halide perovskites: fundamental mechanisms and limits. *ACS Energy Lett*, 2017, **2**:1539–1548.

[19] Yao H, Zhou F, Li Z, *et al*. Strategies for improving the stability of tin-based perovskite (ASnX$_3$) solar cells. *Adv Sci (Weinh)*, 2020, **7**:1903540.

[20] Lanzetta L, Webb T, Zibouche N, *et al*. Degradation mechanism of hybrid tin-based perovskite solar cells and the critical role of tin (IV) iodide. *Nat Commun*, 2021, **12**:2853.

[21] Wang T, Xu X, Li W, *et al*. Simultaneous enhancement of thermoelectric power factor and phase stability of tin-based perovskites by organic cation doping. *ACS Appl Energy Mater*, 2022, **5**:11191–11199.

[22] Liu T, Zhao X, Li J, *et al*. Enhanced control of self-doping in halide perovskites for improved thermoelectric performance. *Nat Commun*, 2019, **10**:5750.

[23] Tang W, Liu T, Fenwick O. High thermoelectric performance based on CsSnI$_3$ thin films with improved stability. *J Mater Chem A*, 2022, **10**:7020–7028.

[24] Qian F, Hu M, Gong J, *et al*. Enhanced thermoelectric performance in lead-free inorganic CsSn$_{1-x}$Ge$_x$I$_3$ perovskite semiconductors. *J Phys Chem C*, 2020, **124**:11749–11753.

[25] Chung I, Song J-H, Im J, *et al*. CsSnI$_3$: semiconductor or metal? High electrical conductivity and strong near-infrared photoluminescence from a single material: high hole mobility and phase-transitions. *J Am Chem Soc*, 2012, **134**:8579–8587.

[26] Monacelli L, Marzari N. First-principles thermodynamics of CsSnI$_3$. *Chem Mater*, 2023, **35**:1702–1709.

[27] Chen M, Ju M-G, Garces HF, *et al*. Highly stable and efficient all-inorganic lead-free perovskite solar cells with native-oxide passivation. *Nat Commun*, 2019, **10**:16.

[28] Werker W. Die Krystallstruktur des Rb$_2$SnJ$_6$ und Cs$_2$SnJ$_6$. *Recl Trav Chim PaysBas*, 1939, **58**:257–258.

[29] Kontos AG, Kaltzoglou A, Siranidi E, *et al*. Structural stability, vibrational properties, and photoluminescence in CsSnI$_3$ perovskite upon the addition of SnF$_2$. *Inorg Chem*, 2017, **56**:84–91.

[30] Huang BX, Tornatore P, Li Y-S. IR and Raman spectroelectrochemical studies of corrosion films on tin. *Electrochim Acta*, 2001, **46**:671–679.

[31] Zhu W, Xin G, Scott SM, *et al*. Deciphering the degradation mechanism of the lead-free all inorganic perovskite Cs$_2$SnI$_6$. *npj Mater Degrad*, 2019, **3**:7.

[32] Wieczorek A, Lai H, Pious J, *et al*. Resolving oxidation states and Sn-halide interactions of perovskites through Auger parameter analysis in XPS. *arXiv preprint arXiv* https://doi.org/10.48550/arXiv.2207.14123, 2022, preprint: not peer reviewed.

[33] Meggiolaro D, Ricciarelli D, Alasmari AA, *et al*. Tin versus lead redox chemistry modulates charge trapping and self-doping in tin/lead iodide perovskites. *J Phys Chem Lett*, 2020, **11**:3546–3556.

[34] Euvrard J, Yan Y, Mitzi DB. Electrical doping in halide perovskites. *Nat Rev Mater*, 2021, **6**:531–549.

[35] Su Y, Song KK, Zhong M, *et al*. Stability and phonon-limited mobility for CsSnI$_3$ and CsPbI$_3$. *J Alloys Compd*, 2021, **889**:161723.

[36] Whall TE, Juzova V. Narrow-band charge transport in SnI$_4$. *J Phys C: Solid State Phys*, 1973, **6**:2329–2336.

[37] Xie H, Hao S, Bao J, *et al*. All-inorganic halide perovskites as potential thermoelectric materials: dynamic cation off-centering induces ultralow thermal conductivity. *J Am Chem Soc*, 2020, **142**:9553–9563.

[38] Yu S, Qian F, Hu M, *et al*. Enhanced thermoelectric performance in inorganic CsSnI$_3$ perovskite by doping with PbI$_2$. *Mater Lett*, 2022, **308**:131127.

[39] Bhui A, Ghosh T, Pal K, *et al*. Intrinsically low thermal conductivity in the n-type vacancy-ordered double perovskite Cs$_2$SnI$_6$: octahedral rotation and anharmonic rattling. *Chem Mater*, 2022, **34**:3301–3310.

[40] Qiu X, Cao B, Yuan S, *et al*. From unstable CsSnI$_3$ to air-stable Cs$_2$SnI$_6$: a lead-free perovskite solar cell light absorber with bandgap of 1.48eV and high absorption coefficient. *Sol Energy Mater Sol Cells*, 2017, **159**:227–234.

[41] Sebastia-Luna P, Pokharel U, Huisman B, *et al*. Vacuum-deposited cesium tin iodide thin films with tunable thermoelectric properties. *ACS Appl Energy Mater*, 2022, **5**:10216–10223.

[42] Baranwal AK, Saini S, Wang Z, *et al*. Interface engineering using Y$_2$O$_3$ scaffold to enhance the thermoelectric performance of CsSnI$_3$ thin film. *Org Electron*, 2020, **76**:105488.

[43] Zheng Y, Fang Z, Shang MH, *et al*. Enhancing the stability of orthorhombic CsSnI$_3$ perovskite via oriented π-conjugated ligand passivation. *ACS Appl Mater Interfaces*, 2020, **12**:34462–34469.

[44] Talbanova N, Bronnikov O, Luchnikov L, *et al*. The buffer-free semitransparent perovskite solar cells with ion-beam sputtered back electrode. *Sol Energy Mater Sol Cells*, 2024, **266**:112683.